

Article

Low-Temperature Processed $\text{TiO}_x/\text{Zn}_{1-x}\text{Cd}_x\text{S}$ Nanocomposite for Efficient $\text{MAPbI}_x\text{Cl}_{1-x}$ Perovskite and PCDTBT:PC₇₀BM Polymer Solar Cells

Binh Duong¹, Khathawut Lohawet¹, Tanyakorn Muangnapoh¹, Hideki Nakajima² , Narong Chanlek², Anirudh Sharma³ , David A. Lewis⁴  and Pisist Kumnorkaew^{1,*} 

¹ National Nanotechnology Center, 111 Thailand Science Park, Paholyothin Road, Klong 1, Klong Luang, Pathumthani 12120, Thailand; bduong07@gmail.com (B.D.); khathawut.loh@nanotec.or.th (K.L.); tanyakorn.mua@nanotec.or.th (T.M.)

² Synchrotron Light Research Institute, 111 University Avenue, Muang District, Nakhon Ratchasima 30000, Thailand; hideki@slri.or.th (H.N.); narong@slri.or.th (N.C.)

³ University of Bordeaux, Laboratoire de Chimie des Polymères Organiques (LCPO), UMR 5629, B8 Allée Geoffroy Saint Hilaire, 33615 Pessac Cedex, France; anirudh.sharma@enscbp.fr

⁴ Flinders Institute for Nanoscale Science and Technology, Flinders University, Adelaide, SA 5042, Australia; david.lewis@flinders.edu.au

* Correspondence: pisist@nanotec.or.th

Received: 20 April 2019; Accepted: 9 May 2019; Published: 3 June 2019



Abstract: The majority of high-performance perovskite and polymer solar cells consist of a TiO_2 electron transport layer (ETL) processed at a high temperature (>450 °C). Here, we demonstrate that low-temperature (80 °C) ETL thin film of $\text{TiO}_x:\text{Zn}_{1-x}\text{Cd}_x\text{S}$ can be used as an effective ETL and its band energy can be tuned by varying the $\text{TiO}_x:\text{Zn}_{1-x}\text{Cd}_x\text{S}$ ratio. At the optimal ratio of 50:50 (vol%), the $\text{MAPbI}_x\text{Cl}_{1-x}$ perovskite and PCBTBT:PC₇₀BM polymer solar cells achieved 9.79% and 4.95%, respectively. Morphological and optoelectronic analyses showed that tailoring band edges and homogeneous distribution of the local surface charges could improve the solar cells efficiency by more than 2%. We proposed a plausible mechanism to rationalize the variation in morphology and band energy of the ETL.

Keywords: electron transport layer; TiO_x ; ZnCdS ; solar cells; perovskite; polymer; scanning Kelvin probe microscopy

1. Introduction

The ever-growing energy demand relies mainly on the combustion of fossil fuel, which continues to cause serious resource depletion and environmental pollution. Solar energy is a proven renewable energy that is environmentally friendly and free from regional restriction. Inorganic solar cells (i.e., Si-based, gallium arsenide, copper indium gallium selenide, cadmium telluride, etc.) offer high efficiency (more than 25%) and stability, however, the technology development is hindered by a sophisticated manufacturing process in addition to the handling of toxic materials [1]. While dye-sensitized, polymer and perovskite solar cells are the emerging photovoltaic devices that are both lightweight and low cost, they however have their own set of problems that inhibit their large-scale production as was highlighted in recent review papers [1–3]. To realize their practical applications, device stability is one of the critical factors that needs to be understood and overcome. Different approaches have been proposed for a more stable polymer [4–6], dye-sensitized and perovskite solar cells [7–11].

Interface engineering can be considered as the most crucial factor in order to achieve high performance and stable solar cells, because it shapes the pathways of photogenerated charge carriers

from an active layer to metal electrodes. Both polymer solar cells and perovskite solar cells can be easily fabricated in n-i-p configuration where electrons are collected at the bottom electrode, or p-i-n configuration where electrons are collected at the top electrode, via simple solution processes. In terms of device performances, p-i-n devices often exhibit more reliable performances and better environmental stability. However, their efficiencies are slightly lower than that of n-i-p structures due to the barrier in Fermi levels at the interface between the electron transport layer and the metal electrode [12]. Significant efforts have been devoted to developing interfacial materials for better band alignment, defect passivation and charge separation. While ZnO [13,14], SnO₂ [15], Al₂O₃ [16], MoO_x [17], core-shell nanoparticles/structures [18], and organic compounds [3,19,20] have all been reported as materials for electron transport layer (ETL), TiO₂ remains the most widely used and essential ETL material for both polymer solar cells and perovskite solar cells owing to the ease of tuning its optical and electrical band gaps. Comprehensive reviews on ETL materials, properties and interface engineering have been reported in recent papers [12,21,22]. Different concepts of tailoring TiO₂ have been proposed and showed promising results including metal-doped TiO₂ [23], amino acid-modified TiO₂ [24], plasmon-mediated TiO₂ [25], or functionalized organic/polymer on TiO₂ [26,27].

Instead of doping TiO₂, synthesizing ETL composite of two metal oxides with appropriate band edges is another approach in facilitating electron transport, offering better efficiency and minimizing recombination rate. ETL composites of SrTiO₃/TiO₂ [28], BaTiO₃/TiO₂ [29], and In₂O₃/TiO₂ [30] have been shown to improve the overall device efficiency. Nevertheless, it is critical to further optimize the suitable mixing ratio (molar ratio, volume ratio) in order to achieve high power conversion efficiency. Controlling film thickness and morphology are the main challenges in using nanocomposites as ETL. It is also unclear how work function would vary at nanometer level when two semiconducting metal oxides are mixed together and the influence of lateral inhomogeneity of work function on the device performance.

In addition, the formation of crystalline TiO₂ requires high temperature annealing (500 °C) which is not suitable for fabricating devices on flexible substrates, as well as for many other practical applications. Several groups have addressed this issue by developing low-temperature processes. Kim et al. found that the devices made of ultra-thin amorphous TiO_x by atomic layer deposition are more stable than crystalline TiO₂ [31,32]. Recently, Deng et al. reported that high efficiency perovskite solar cells could be achieved using TiO_x processed at room-temperature [33]. Another study by Wang et al. demonstrated that efficient perovskite devices made of ETL nanocomposites of graphene/TiO₂ could be processed at 150 °C [34].

Here, we show that low-temperature (80 °C) processed TiO_x:Zn_{1-x}Cd_xS (T:Z) can be used as an effective ETL in both p-i-n perovskite and polymer solar cells. Zn_{1-x}Cd_xS was chosen due to the ease of synthesis and highly tunable bandgap by varying Zn/Cd molar ratios [35]. We examined performances of the p-i-n devices using different loadings of Zn_{1-x}Cd_xS in TiO_x and carried out electrochemical impedance spectroscopy, ultraviolet photoelectron spectroscopy (UPS) and scanning Kelvin probe microscopy (SKPM) measurements. The local morphology with corresponding work function obtained from SKPM can shed more light into the fundamental understanding of electron transport layer in solar cells.

2. Materials and Methods

2.1. Chemical Preparation

2.1.1. Zn_{1-x}Cd_xS Nanoparticles Synthesis

During the process, 0.55 g of zinc acetate (99.99%, Ajax Finechem, New South Wales, Australia) and 0.33 g of cadmium acetate (99.99% Asia Pacific Specialty Chemicals Limited, New South Wales, Australia) were dissolved in 25 mL of DI water and stirred for 15 min. Another solution of 0.65 g thioacetamide (99.0%, Sigma Aldrich, MO, USA) and 0.6 g of polyvinylpyrrolidone (99.0%, Sigma Aldrich, MO, USA) in 25 mL DI water were prepared. Both solutions were mixed and stirred

at room temperature for 30 min. The mixture was heated with 700 W microwave (Sharp Cooperation, Osaka, Japan) radiation for 3 min. $Zn_{1-x}Cd_xS$ nanopowder was filtered and rinsed with 2-butanol [36]. The nanopowder was dried at 250 °C for 2 h and calcined at 500 °C for 1 h. Suspension of 0.4 mg/mL $Zn_{1-x}Cd_xS$ in 2-butanol was used in all experiments.

2.1.2. TiO_x Synthesis

During the synthesis, 2.7 mL titanium (IV) butoxide (97%, Sigma Aldrich, MO, USA), 0.57 mL ethyl acetoacetate (99%, Sigma Aldrich), 57 μ L 2,4-pentanedione (99%, Sigma Aldrich, MO, USA) and 57 μ L 2,3-butanedione (97%, Sigma Aldrich, MO, USA) were mixed and stirred at room temperature overnight [37].

2.1.3. Polymer (PCDTBT:PC₇₀BM) Ink Formulation

For PCDTBT:PC₇₀BM ink formation, 8 mg of PCDTBT (Ossila Ltd., Sheffield, UK) and 32 mg of PC₇₀BM (Ossila Ltd., Sheffield, UK) were dissolved in 1 mL anhydrous dichlorobenzene (Sigma Aldrich, MO, USA). This PCDTBT:PC₇₀BM is used for polymer solar cells. For perovskite solar cells, PC₇₀BM solution was prepared by dissolving 50 mg of PC₇₀BM into 1 mL anhydrous dichlorobenzene (Sigma Aldrich, MO, USA). Both solutions were then stirred at 60 °C for 1 h [17].

2.1.4. Perovskite (MAPbI_xCl_{3-x}) Ink Formulation

For MAPbI_xCl_{3-x} ink formation, 2.4 g of MAI (Ossila Ltd., Sheffield, UK) and 1.4 g PbCl₂ (Sigma Aldrich, MO, USA) were mixed and stirred in 5 mL anhydrous dimethylformamide (Sigma Aldrich, MO, USA) at 70 °C for 2 h [38].

2.2. Device Fabrication

Polymer and perovskite solar cells were fabricated on pre-patterned ITO glass (Luminescence Technology Corporation, Taipei, Taiwan, 25 × 25 mm², 5 Ω /sq). Prior to the fabrication, the substrates were cleaned by ultrasonication under detergent, DI water, acetone, and isopropyl alcohol sequentially. The substrates were further exposed under 395 UV light for 20 min.

Convective deposition [39] or spin coating method was used for depositing of hole transporting, photoactive, and electron transporting layers. A cleaned glass microscope slide (75 × 25 × 1 mm³, Fisher PA, Charlotte, NC, USA) was used as a deposition blade and placed at 45° with respect to the patterned ITO substrate. PEDOT:PSS was used as the hole transporting layer for both solar cells. 20 μ L of PEDOT:PSS (100 nm) were coated twice by convective deposition at the speed of 3000 μ m/s. The coated substrate was annealed on a hot plate at 120 °C for 30 min in the ambient environment (%RH 50-60). The polymer solar cell fabrication was continued under ambient conditions while the PEDOT:PSS coated substrates were transferred to a glove box for perovskite solar cell fabrication.

For polymer solar cell with ITO/PEDOT:PSS/PCDTBT:PC₇₀BM/ TiO_x /Al structure, 20 μ L PCDTBT:PC₇₀BM (80 nm) were convectively deposited at the speed of 750 μ m/s and left in air for 3 min followed by the deposition of 20 μ L TiO_x solution with various $Zn_{1-x}Cd_xS$ suspension ratio. The coated films (20 nm) were annealed at 80 °C.

For perovskite solar cell with ITO/PEDOT:PSS/CH₃NH₃PbI_xCl_{3-x}/PC₇₀BM/ TiO_x /Al structure, 40 μ L perovskite ink were deposited with spin coating technique with 2250 rpm for 30 s. The substrate and ink were kept at 70 °C before the deposition. The perovskite (300 nm) coated substrate was annealed at 100 °C on a hot plate for 90 min. Following this, 35 μ L of 50mg/mL PC₇₀BM solution were spin casted onto the perovskite film at 1500 rpm for 30 s. Then, 200 μ L TiO_x solution with various $Zn_{1-x}Cd_xS$ suspension ratio were spin casted (20 nm) with 2500 rpm for 30 s. The multilayer films were then annealed at 80 °C for 30 min in a glove box.

Aluminum metal electrode (80 nm) was deposited on top of the TiO_x layer to complete the polymer and perovskite solar cell fabrication. Four independent cells with 0.1 cm² active area per cell were fabricated on the patterned ITO substrate.

2.3. Characterization

Surface morphologies were characterized by atomic force microscope (NanoWizard 3 NanoScience, JPK Instruments, Berlin, Germany). Bruker OSCM-PT-R3 AFM probes (Bruker Nano, CA, USA) were used. The solar cell performance was measured using 0.1 cm² mask under 100 mW/cm² and 1.5 AM filter (Abet Technologies, Milford, CT, USA). The light intensity was calibrated by 4 cm² solar cell reference (VLSI Standards, Mountain View, CA, USA). I-V measurements were conducted using source measurement unit (PXI-4130, National Instrument, Austin, TX, USA with 10 mV scan step from 1 V to −1 V. Incident photon-to-current efficiency IPCE was measured using QEPVSI-b (Newport Corporation, Irvine, CA, USA). Impedance spectroscopy and Mott-Shockley (M-S) measurements were carried out using CHI 660E electrochemical work station (CH Instruments, Bee Cave, TX, USA). For M-S measurement, a small AC voltage of 5 mV was applied under constant illumination to measure device impedance as a function of frequency (100 Hz to 1 MHz). UPS was carried out at the Synchrotron Light Research Institute.

3. Results and Discussion

To determine the best loading ratio of Zn_{1-x}Cd_xS in TiO_x in both polymer and perovskite solar cells, we fabricated p-i-n cell structures using various volumetric mixing ratios of TiO_x:Zn_{1-x}Cd_xS dispersions as 100:0 (T100), 75:25 (T75:Z25), 50:50 (T50:Z50), 25:75 (T25:Z75), 0:100 (Z100). Figure 1a shows SEM cross-sectional image of the device structures. The perovskite solar cells made of T100, T75:Z25, T50:Z50, T25:Z75 and Z100 achieved the efficiencies of 7.74%, 9.47%, 9.79%, 8.07% and 6.74%, respectively. Polymer solar cells share similar trends with perovskite devices, namely 4.22% (T100), 4.40% (T75:Z25), 4.95% (T50:Z50), 3.63% (T25:Z75) and 2.93% (Z100). Incorporating Zn_{1-x}Cd_xS shows an increase in current density from 15 mA/cm² to 18 mA/cm² for perovskite solar cells (Figure 1b) and from 8 mA/cm² to 11 mA/cm² for polymer solar cells (Table 1) and Figure S1 indicating better carrier extraction from the active layer after ETL modification. Further details on perovskite solar cell performances are shown in Table 2. Negligible hysteresis for this p-i-n perovskite solar cell was observed after forward-reverse scan study as shown in Figure S2 in supplementary information. The results agree well with previous studies [40–42].

EIS and Mott-Schottky measurements were carried out to understand the recombination losses and charge transport properties upon mixing Zn_{1-x}Cd_xS into TiO_x. Figure 1c shows Nyquist plots for perovskite solar cells and polymer solar cells at different loading of Zn_{1-x}Cd_xS. The high frequency intercept of the Nyquist plot attributed to the series resistance and the low-frequency intercept corresponds to the recombination resistance (R_{rec}). As R_{rec} gets larger, lower leakage current and recombination occur at the surface. It was clearly observed that R_{rec} increased for devices containing Zn_{1-x}Cd_xS, which had lower recombination losses. In addition, the lifetime of free carriers (τ) could be calculated from the maximum frequency (f_m) obtained from Bode plot as shown in Figure 1d by

$$\tau = \frac{1}{2\pi f_m} \quad (1)$$

The carrier lifetime increased from 46 μ s to 68 μ s and to 82 μ s as Zn_{1-x}Cd_xS content increased from 0 to 100%. It is also well known that the interfacial charge density is inversely proportional to the slope of the Mott-Schottky plots (Figure 1e) as follows:

$$\frac{1}{C^2} = \frac{2}{e\epsilon_0\epsilon_r N A^2} (V - V_{fb} - \frac{k_B T}{e}) \quad (2)$$

where C is capacitance, ϵ_0 is vacuum permittivity, ϵ_r is dielectric constant of material, N is charge carrier density, A is electrode area, V is applied potential, V_{fb} is flat band potential, k_B is Boltzmann constant, T is absolute room temperature and e is elementary charge of electron. As the charge carrier density is smaller than 5×10^{20} cm⁻³ [43], the difference in flat band potential is negligible.

Assuming an equivalent dielectric constant for all devices under illumination, the slopes of T100, T75:Z25, T50:Z50, T25:Z75 and Z100 are -2.2×10^{10} , -2.3×10^{10} , -2.4×10^{10} , -1.8×10^{10} , -1.0×10^{10} respectively, indicating the highest interfacial charge density and resulting in the highest current density.

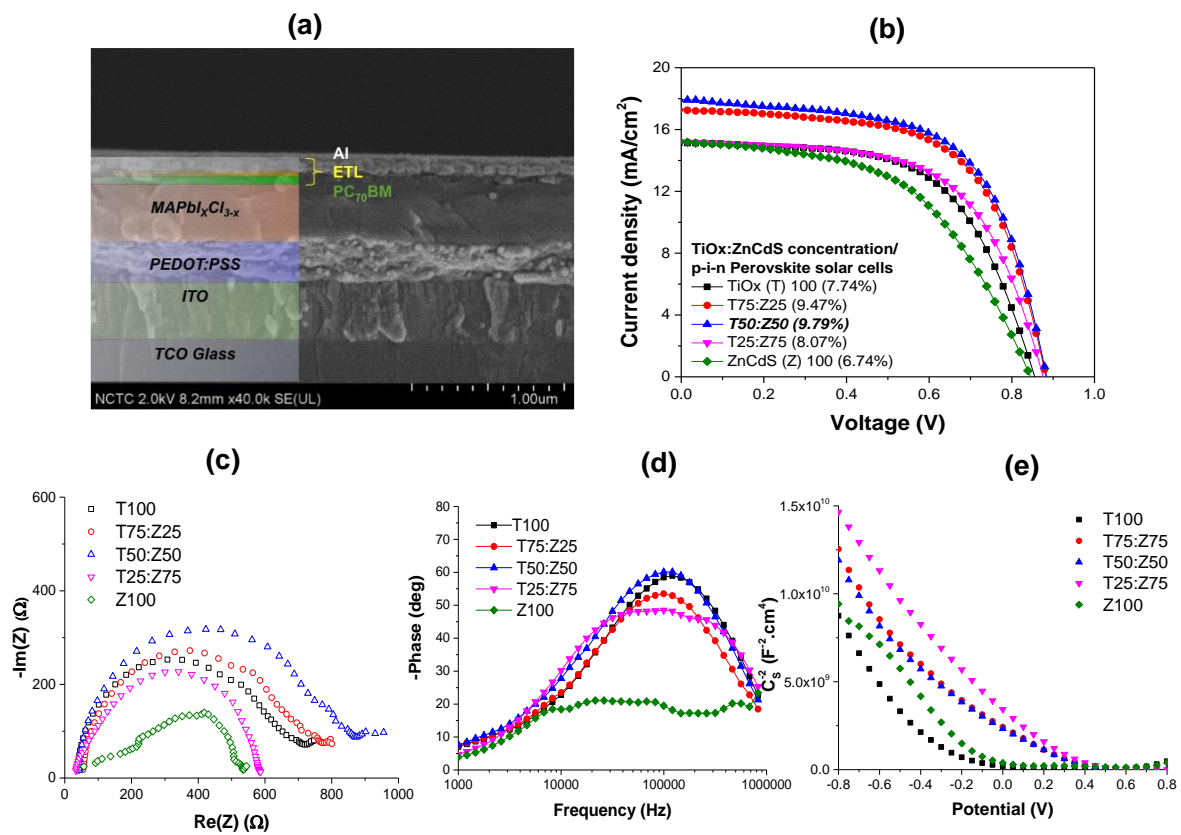


Figure 1. (a) SEM cross-sectional image, (b) J-V characteristics of perovskite solar cells, (c) Nyquist plot, (d) Bode plot and (e) Mott-Schottky plot of perovskite solar cells fabricated from different ratio of $\text{TiO}_x:\text{Zn}_{1-x}\text{Cd}_x\text{S}$.

Table 1. Performances of polymer solar cells fabricated from different T:Z ETL.

TiO _x : ZnCdS Conc. (%)	V _{oc} (V)	J _{sc} (mA/cm ²)	FF	PCE (%)
T100	0.879 (0.869 ± 0.008)	8.79 (8.67 ± 0.484)	0.55 (0.52 ± 0.028)	4.22 (3.94 ± 0.280)
T75:Z25	0.869 (0.867 ± 0.002)	10.59 (10.18 ± 0.465)	0.48 (0.47 ± 0.007)	4.40 (4.18 ± 0.245)
T50:Z50	0.910 (0.896 ± 0.012)	10.35 (10.25 ± 0.191)	0.53 (0.52 ± 0.013)	4.95 (4.77 ± 0.138)
T25:Z75	0.849 (0.844 ± 0.005)	8.55 (8.48 ± 0.214)	0.50 (0.50 ± 0.009)	3.63 (3.56 ± 0.086)
Z100	0.869 (0.863 ± 0.004)	8.69 (8.81 ± 0.166)	0.39 (0.38 ± 0.010)	2.93 (2.90 ± 0.030)

Table 2. Performances of perovskite solar cells fabricated from different T:Z ETL.

TiO _x : ZnCdS Conc. (%)	V _{oc} (V)	J _{sc} (mA/cm ²)	FF	PCE (%)
T100	0.859 (0.848 ± 0.007)	15.14 (15.72 ± 0.391)	0.60 (0.57 ± 0.015)	7.74 (7.65 ± 0.09)
T75:Z25	0.879 (0.880 ± 0.003)	17.31 (16.22 ± 1.922)	0.62 (0.62 ± 0.009)	9.47 (8.79 ± 1.024)
T50:Z50	0.889 (0.884 ± 0.003)	17.99 (17.82 ± 0.139)	0.61 (0.61 ± 0.001)	9.79 (9.67 ± 0.090)
T25:Z75	0.879 (0.875 ± 0.009)	15.19 (15.13 ± 1.177)	0.60 (0.57 ± 0.042)	8.07 (7.58 ± 0.590)
Z100	0.849 (0.844 ± 0.007)	15.19 (13.61 ± 3.159)	0.52 (0.50 ± 0.050)	6.74 (5.81 ± 1.796)

To better understand the nature of the starting materials, we performed detailed characterizations of TiO_x, Zn_{1-x}Cd_xS and their nanocomposites. SEM images and EDS spectra (Figure S3) to confirm that the prepared nanocomposites form uniform, smooth thin films and addition of Zn_{1-x}Cd_xS in TiO_x does not effect on the morphology of the films. TEM images (Figure S4) reveal that the TiO_x is in amorphous form with small amount of anatase crystals of TiO₂ while Zn_{1-x}Cd_xS is fully crystalline with crystallite size of about 5 nm. UV-Vis spectra and Tauc plots are shown in Figure S5. The band gaps calculated from Tauc plot of T100 and Z100 thin films are 3.7 and 2.5 eV, respectively, which are in good agreement with the band gap of TiO_x and Zn_{1-x}Cd_xS reported in the literatures [33,35]. The band gap values obtained from highest slopes in the Tauc plot of T75:Z25, T50:Z50, T25:Z75 films share the same value of 3.47 eV, which is lower than that of the pure T100 film. The nanocomposite ETL films also exhibit minor slopes, indicating indirect transitions or existence of gap states [44]. The indirect band gap is shifted from 3.0 eV for T75:Z25 to 3.1 eV for T50:Z50 to 3.25 eV for T25:Z75.

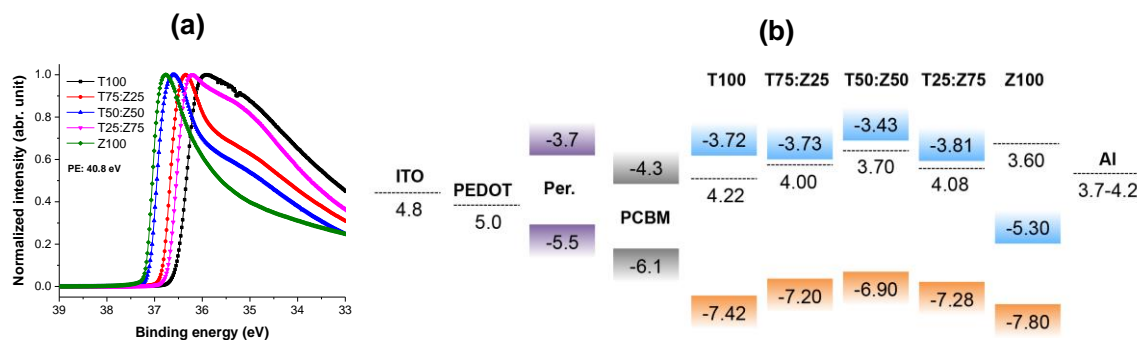


Figure 2. (a) UPS spectra and (b) proposed energy band diagram of TiO_x:Zn_{1-x}Cd_xS nanocomposite films. Energy levels of ITO, PEDOT:PSS, perovskite, PC₇₀BM and Al were taken from other studies [3,32]. Photon energy (PE) is 40.8 eV.

Ultraviolet photoelectron spectroscopy (UPS) was used to characterize the work function and valence band energy of TiO_x:Zn_{1-x}Cd_xS electron transport layer. UPS spectra of 10 nm T:Z thin films coated on silicon substrates are shown in Figure 2a. The effective work functions of the films were obtained by subtracting the source energy (40.8 eV) by the energy difference (ΔKE) between the low kinetic energy edge (*LKE*) and the spectrometer/sample Fermi level:

$$\phi = 40.8 - \Delta KE \tag{3}$$

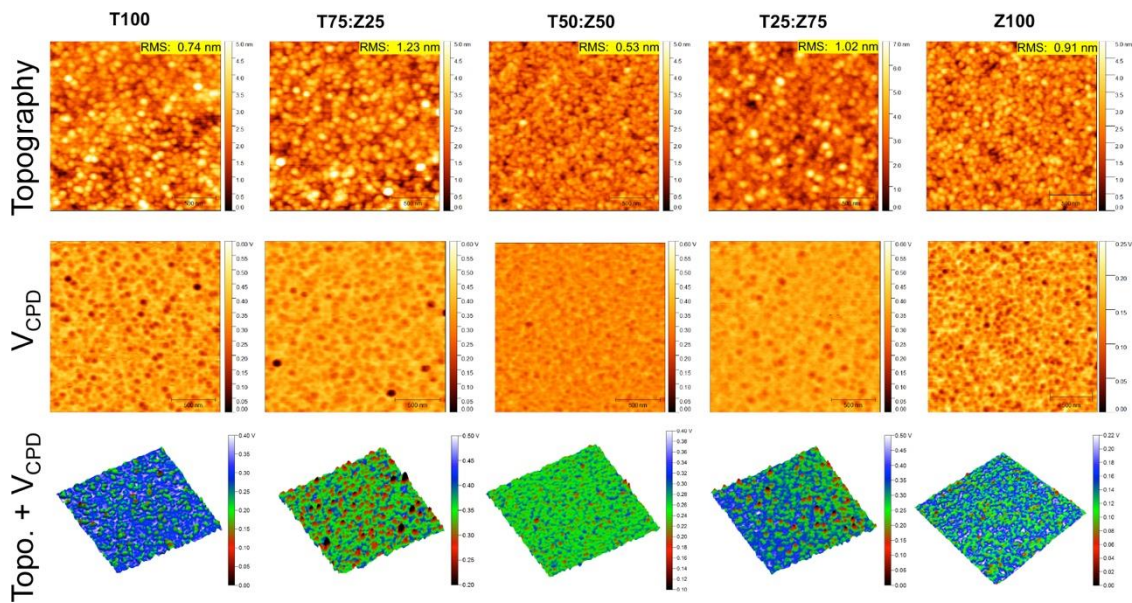


Figure 3. Topography, contact potential difference (V_{CPD}) and 3D map highlight variation in local charge distribution of $TiO_x:Zn_{1-x}Cd_xS$ nanocomposite films. Scan area: $2\mu m \times 2\mu m$.

The valence band energy (E_{VB}) was estimated by subtracting the source energy (40.8 eV) by the energy difference ($\Delta KE'$) between the LKE and the high kinetic energy (HKE) edge for photoemission as below:

$$\phi = 40.8 - \Delta KE' \quad (4)$$

The work functions of T100, T75:Z25, T50:Z50, T25:Z75 and Z100 thin films with respect to the vacuum level are 4.22, 4.00, 3.70, 4.08 and 3.60 eV, respectively (Table S1). The valence band energy of T100, T75:Z25, T50:Z50, T25:Z75 and Z100 thin films with respect to the vacuum level are -7.42 , -7.20 , -6.90 , -7.28 and -7.80 eV, respectively. Figure 2b shows a proposed general band energy diagram of $TiO_x:Zn_{1-x}Cd_xS$ nanocomposite electron transport layer. The band energy levels of ITO, PEDOT, perovskite/PCDTBT, PC₇₀BM and Al were taken from other studies [12,32].

Scanning Kelvin probe microscopy (SKPM) is an effective technique to monitor simultaneously morphology/topography and contact potential difference (V_{CPD}) between the atomic force microscopy tip and sample surface. When the AFM tip and sample is far apart and not connected electrically, their Fermi levels are different. As the AFM tip approaches the sample surface, an electrical force is induced between the tip and the sample surface, brought their Fermi levels to line-up and formed contact potential difference (CPD). To measure this CPD, an external bias is applied at the contact area until the surface potential difference between the tip and the sample becomes zero. The magnitude of the applied bias equals to the work function difference between the tip and the sample, which means the work function of the sample can be calculated once the work function of the tip is known. The measured CPD is defined as the difference in work function between a tip and a sample as follows:

$$V_{CPD} = \frac{\phi_{tip} - \phi_{sample}}{e^-} \quad (5)$$

where V_{CPD} is the CPD between the tip and the sample, ϕ_{tip} and ϕ_{sample} are the work functions of the tip and the sample, respectively and e^- is the elementary charge. To obtain the work function of the AFM tip, freshly cleaved highly oriented pyrolytic graphite (HOPG, $\phi = 4.6$ eV) and thermally evaporated gold thin film (Au, $\phi = 5.1$ eV) were used. For all measurements, the substrate was grounded. Topographical and potential maps of the pure TiO_x , $Zn_{1-x}Cd_xS$ and mixed $TiO_x:Zn_{1-x}Cd_xS$ thin films are shown in Figure 3. Three-dimensional maps combining topographic and V_{CPD} data clearly show that the T50:Z50 film possesses the least variation in surface potential compared to

other ETL films. Potential histograms of all samples are shown in Figure 4a. The work function of T50:Z50 is 3.75 ± 0.28 eV compared to 3.47 ± 0.44 eV of T100 and 3.77 ± 0.29 eV of Z100, which are comparable to UPS data. FWHM value of T50Z50 has minimum value, indicating the least variation in work function at nanoscale level. It is expected that the work function values of ETL composite films obtained from SKPM technique are slightly lower than those obtained from UPS method due to water adsorption and hydrocarbon contamination (Tables S1 and S2). Although the work function value of T100 film estimated from SKPM method is about 0.4 eV lower than that of UPS value, it is in good agreement with plasma enhanced atomic layer deposited TiO_x films reported in Kim's study [32]. Figure 4b–f shows profiles at three different locations from SKPM image of T25:Z75 film, which indicates that the surface potential depends on the film roughness. As the tip scanned over a particle, the height abruptly increased about 5 nm, and the local V_{CPD} decreased about 200 mV, leading to an increase at the local work function. The distribution of charges at the surface and potential step can be attributed to crystallographic orientation and atomic relaxation [45]. It is possible that electronegative character of $\text{Zn}_{1-x}\text{Cd}_x\text{S}$ results in a partial electron transfer with TiO_x that leads to an increase in local work function [45]. When the height decreased about 3 nm, the local V_{CPD} increased about 100 mV. Within 1–2 nm variation in height, the local charge distribution could be fluctuated about 50 mV. The overall results indicate that an effective ETL composites of mixed metal oxides should have root mean square roughness of about 0.5 nm and scanning probe microscopy can be used as an effective tool to predict the homogeneity of local charges.

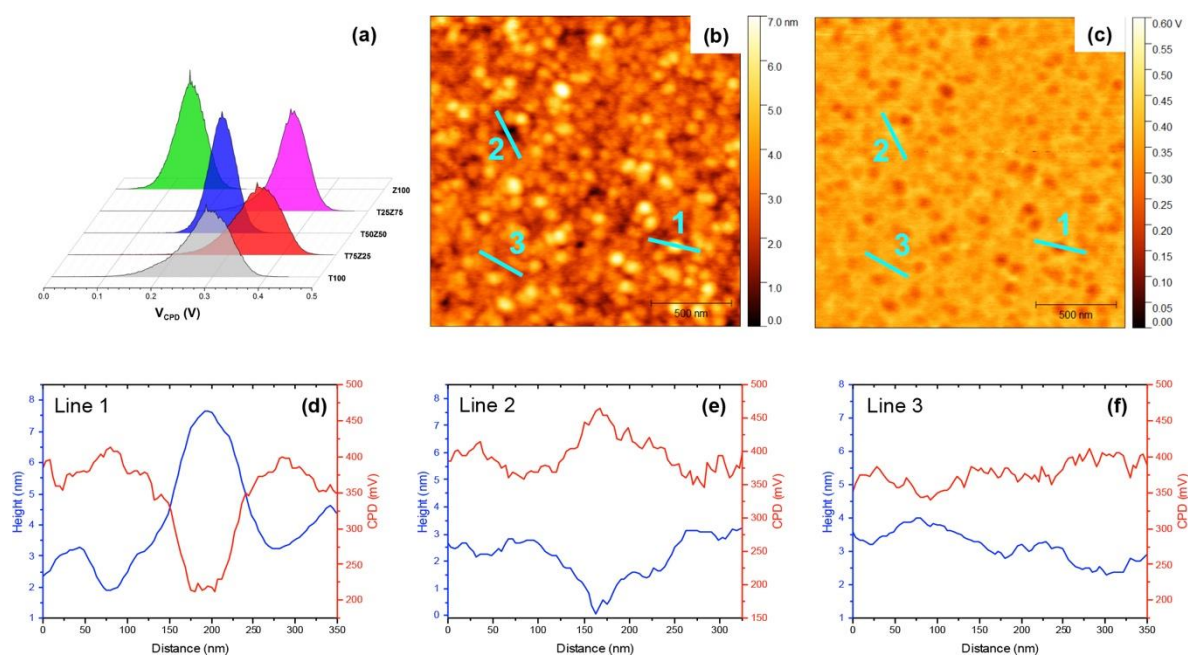


Figure 4. (a) Surface potential V_{CPD} histograms of $\text{TiO}_x:\text{Zn}_{1-x}\text{Cd}_x\text{S}$ nanocomposite films, (b) topography and (c) its corresponding surface potential image, (d–f) Profiles extracted from topography and surface potential at three different locations of T25:Z75 film.

We suggest the following mechanism to rationalize for morphological and electronic variation of $\text{TiO}_x:\text{Zn}_{1-x}\text{Cd}_x\text{S}$ nanocomposite films. In pure TiO_x film, nanocrystals can be formed from Ti-O monomers via hydrolysis and condensation reactions which are strongly dependent on reaction temperature. Solvent evaporates, supersaturates the polymeric precursor solution and leads to the formation of a large number of Ti-O species. At low temperature (80°C), the nuclei impinge on each other and impede further grain growth via diffusion, resulting in a relatively smooth film of small grains (RMS: 0.7 nm), but the mixture of amorphous and crystalline phases (dominantly amorphous phase) leads to broad distribution of work function (3.47 ± 0.44 eV). Pure $\text{Zn}_{1-x}\text{Cd}_x\text{S}$

film follows similar mechanism as TiO_x film, however, there is no polymeric precursor. The pure $\text{Zn}_{1-x}\text{Cd}_x\text{S}$ film is in smooth, crystalline phase (RMS: 0.9 nm), resulting in narrow distribution of work function (3.77 ± 0.29 V). When preexisting $\text{Zn}_{1-x}\text{Cd}_x\text{S}$ seeds are present in the initial stage of the synthesis, the Ti-O species are immobilized onto the seed crystals to overcome the activation energy barrier for nucleation, leading to the formation of bigger grains compared to that of pure films and creating an ordered electronic network of TiO_x surrounding the grains. For T75Z25 film, the density of $\text{Zn}_{1-x}\text{Cd}_x\text{S}$ in the composite film is too low, resulting in rougher film due to scattering of the large crystalline grains. For T25Z75 film, the density of $\text{Zn}_{1-x}\text{Cd}_x\text{S}$ in the composite film is too high, the grains are interconnected by the polymer chains similar to the mechanism proposed by Yang's group [11], however, the volume of TiO_x is not enough to bridge the gaps between grains, resulting in a rough surface. For T50Z50 film, the density of $\text{Zn}_{1-x}\text{Cd}_x\text{S}$ is optimal in the TiO_x matrix, the distribution of seed crystals and its proximity interaction with surrounding polymer chains is the most effective, resulting in the smoothest film among all. As the morphology and internal structures of ETL films are tuned by addition of $\text{Zn}_{1-x}\text{Cd}_x\text{S}$, the band energy of ETL is simultaneously modified due to presence of $\text{Zn}_{1-x}\text{Cd}_x\text{S}$ energy states and surrounding TiO_x electronic network, which are supported by UV-Vis, UPS and SKPM results. Ultimately, appropriate addition of $\text{Zn}_{1-x}\text{Cd}_x\text{S}$ can be used to maximize the optoelectronic output and stability of ETL film and the corresponding devices.

4. Conclusions

This study has demonstrated that efficient perovskite and polymer solar cells were successfully fabricated using low-temperature processed $\text{TiO}_x:\text{Zn}_{1-x}\text{Cd}_x\text{S}$ thin film as an electron transport layer. The ETL band energy can be simply tuned by varying $\text{TiO}_x:\text{Zn}_{1-x}\text{Cd}_x\text{S}$ ratio. The addition of $\text{Zn}_{1-x}\text{Cd}_x\text{S}$ in TiO_x lowers band gap, alters valence band positions and work function levels, reduces recombination at interfaces and increases charge carrier lifetime. The impact of local surface potential homogeneity of $\text{TiO}_x:\text{Zn}_{1-x}\text{Cd}_x\text{S}$ nanocomposite electron transport layer on the performance of p-i-n perovskite and polymer solar cells has been revealed. Together with tailoring band edges, a homogeneous distribution of the local surface charges has been shown to improve solar cells' efficiency by more than 2%.

Supplementary Materials: The following are available online at <http://www.mdpi.com/2073-4360/11/6/980/s1>.

Author Contributions: The manuscript was written through contributions of all authors. All authors have given approval to the final version of the manuscript.

Funding: This work has been supported by the Thailand National Science and Technology Development Agency (P1750159) and Thailand Research Fund (TRG 880194).

Acknowledgments: The authors acknowledge the expertise, equipment and support provided by Microscopy Australia and the Australian National Fabrication Facility (ANFF) at the South Australian nodes under the National Collaborative Research Infrastructure Strategy. The authors thank Watinee Kharnwong, Australian Embassy in Bangkok for promoting academic collaboration between NANOTEC Thailand and Flinders University Australia. The authors also thank Norawit Krainara, Burapha University for ZnCdS synthesis instruction.

Conflicts of Interest: The authors declare no conflict of interest.

References

1. Hou, W.; Xiao, Y.; Han, G.; Lin, J.-Y. The Applications of Polymers in Solar Cells: A Review. *Polymers* **2019**, *11*, 143. [CrossRef] [PubMed]
2. Biniak, L.; Nielsen, C.B. Organic Photovoltaics: More than Ever, an Interdisciplinary Field. *Polymers* **2016**, *8*, 70. [CrossRef] [PubMed]
3. Malinkiewicz, O.; Yella, A.; Lee, Y.H.; Espallargas, G.M.; Graetzel, M.; Nazeeruddin, M.K.; Bolink, H.J. Perovskite solar cells employing organic charge-transport layers. *Nature Photonics* **2014**, *8*, 128–132. [CrossRef]
4. Sai-Anand, G.; Gopalan, A.-I.; Lee, K.-P.; Venkatesan, S.; Qiao, Q.; Kang, B.-H.; Lee, S.-W.; Lee, J.-S.; Kang, S.-W. Electrostatic nanoassembly of contact interfacial layer for enhanced photovoltaic performance in polymer solar cells. *Solar Energy Mater. Solar Cells* **2016**, *153*, 148–163. [CrossRef]

5. Sai-Anand, G.; Gopalan, A.-I.; Lee, K.-P.; Venkatesan, S.; Kang, B.-H.; Lee, S.-W.; Lee, J.-S.; Qiao, Q.; Kwon, D.-H.; Kang, S.-W. A futuristic strategy to influence the solar cell performance using fixed and mobile dopants incorporated sulfonated polyaniline based buffer layer. *Solar Energy Mater. Solar Cells* **2015**, *141*, 275–290. [[CrossRef](#)]
6. Gopalan, S.-A.; Gopalan, A.-I.; Vinu, A.; Lee, K.-P.; Kang, S.-W. A new optical-electrical integrated buffer layer design based on gold nanoparticles tethered thiol containing sulfonated polyaniline towards enhancement of solar cell performance. *Solar Energy Mater. Solar Cells* **2018**, *174*, 112–123. [[CrossRef](#)]
7. Bella, F.; Lamberti, A.; Bianco, S.; Tresso, E.; Gerbaldi, C.; Pirri, C.F. Floating Photovoltaics: Floating, Flexible Polymeric Dye-Sensitized Solar-Cell Architecture: The Way of Near-Future Photovoltaics (Adv. Mater. Technol. 2/2016). *Adv. Mater. Technol.* **2016**, *1*. [[CrossRef](#)]
8. Wang, D.; Zhang, L.; Deng, K.; Zhang, W.; Song, J.; Wu, J.; Lan, Z. Influence of Polymer Additives on the Efficiency and Stability of Ambient-Air Solution-Processed Planar Perovskite Solar Cells. *Energy Technol.* **2018**, *6*, 2380–2386. [[CrossRef](#)]
9. Abate, A.; Correa-Baena, J.-P.; Saliba, M.; Su'ait, M.S.; Bella, F. Perovskite Solar Cells: From the Laboratory to the Assembly Line. *Chem. Eur. J.* **2018**, *24*, 3083–3100. [[CrossRef](#)]
10. Imperiyka, M.; Ahmad, A.; Hanifah, S.A.; Bella, F. A UV-prepared linear polymer electrolyte membrane for dye-sensitized solar cells. *Phys. B Condens. Matter* **2014**, *450*, 151–154. [[CrossRef](#)]
11. Han, T.-H.; Lee, J.-W.; Choi, C.; Tan, S.; Lee, C.; Zhao, Y.; Dai, Z.; De Marco, N.; Lee, S.-J.; Bae, S.-H.; et al. Perovskite-polymer composite cross-linker approach for highly-stable and efficient perovskite solar cells. *Nat. Commun.* **2019**, *10*, 520. [[CrossRef](#)]
12. Bai, Y.; Meng, X.; Yang, S. Interface Engineering for Highly Efficient and Stable Planar p-i-n Perovskite Solar Cells. *Adv. Energy Mater.* **2018**, *8*. [[CrossRef](#)]
13. Ferreira, S.R.; Lu, P.; Lee, Y.-J.; Davis, R.J.; Hsu, J.W.P. Effect of Zinc Oxide Electron Transport Layers on Performance and Shelf Life of Organic Bulk Heterojunction Devices. *J. Phys. Chem. C* **2011**, *115*, 13471–13475. [[CrossRef](#)]
14. Yang, G.; Tao, H.; Qin, P.; Ke, W.; Fang, G. Recent progress in electron transport layers for efficient perovskite solar cells. *J. Mater. Chem. A* **2016**, *4*, 3970–3990. [[CrossRef](#)]
15. Zhao, X.; Tao, L.; Li, H.; Huang, W.; Sun, P.; Liu, J.; Liu, S.; Sun, Q.; Cui, Z.; Sun, L.; et al. Efficient Planar Perovskite Solar Cells with Improved Fill Factor via Interface Engineering with Graphene. *Nano Lett.* **2018**, *18*, 2442–2449. [[CrossRef](#)]
16. Dong, X.; Fang, X.; Lv, M.; Lin, B.; Zhang, S.; Ding, J.; Yuan, N. Improvement of the humidity stability of organic-inorganic perovskite solar cells using ultrathin Al₂O₃ layers prepared by atomic layer deposition. *J. Mater. Chem. A* **2015**, *3*, 5360–5367. [[CrossRef](#)]
17. Sun, Y.; Takacs, C.J.; Cowan, S.R.; Seo, J.H.; Gong, X.; Roy, A.; Heeger, A.J. Efficient, Air-Stable Bulk Heterojunction Polymer Solar Cells Using MoO_x as the Anode Interfacial Layer. *Adv. Mater.* **2011**, *23*, 2226–2230. [[CrossRef](#)]
18. Han, G.S.; Chung, H.S.; Kim, B.J.; Kim, D.H.; Lee, J.W.; Swain, B.S.; Mahmood, K.; Yoo, J.S.; Park, N.-G.; Lee, J.H.; et al. Retarding charge recombination in perovskite solar cells using ultrathin MgO-coated TiO₂ nanoparticulate films. *J. Mater. Chem. A* **2015**, *3*, 9160–9164. [[CrossRef](#)]
19. Seo, J.; Park, S.; Kim, Y.C.; Jeon, N.J.; Noh, J.H.; Yoon, S.C.; Seok, S.I. Benefits of very thin PCBM and LiF layers for solution-processed p-i-n perovskite solar cells. *Energy Environ. Sci.* **2014**, *7*, 2642–2646. [[CrossRef](#)]
20. Jiang, M.; Niu, Q.; Tang, X.; Zhang, H.; Xu, H.; Huang, W.; Yao, J.; Yan, B.; Xia, R. Improving the Performances of Perovskite Solar Cells via Modification of Electron Transport Layer. *Polymers* **2019**, *11*, 147. [[CrossRef](#)]
21. Mahmood, K.; Sarwar, S.; Mehran, M.T. Current status of electron transport layers in perovskite solar cells: Materials and properties. *RSC Adv.* **2017**, *7*, 17044–17062. [[CrossRef](#)]
22. Po, R.; Carbonera, C.; Bernardi, A.; Camaioni, N. The role of buffer layers in polymer solar cells. *Energy Environ. Sci.* **2011**, *4*, 285–310. [[CrossRef](#)]
23. Qin, P.; Domanski, A.L.; Chandiran, A.K.; Berger, R.; Butt, H.-J.; Dar, M.I.; Moehl, T.; Tetreault, N.; Gao, P.; Ahmad, S.; et al. Yttrium-substituted nanocrystalline TiO₂ photoanodes for perovskite based heterojunction solar cells. *Nanoscale* **2014**, *6*, 1508–1514. [[CrossRef](#)] [[PubMed](#)]
24. Shih, Y.C.; Wang, L.Y.; Hsieh, H.C.; Lin, K.F. Enhancing the photocurrent of perovskite solar cells via modification of the TiO₂/CH₃NH₃PbI₃ heterojunction interface with amino acid. *J. Mater. Chem. A* **2015**, *3*, 9133–9136. [[CrossRef](#)]

25. Yuan, Z.; Wu, Z.; Bai, S.; Xia, Z.; Xu, W.; Song, T.; Wu, H.; Xu, L.; Si, J.; Jin, Y.; et al. Hot-Electron Injection in a Sandwiched TiO_x-Au-TiO_x Structure for High-Performance Planar Perovskite Solar Cells. *Adv. Energy Mater.* **2015**, *5*, 1500038. [[CrossRef](#)]
26. Abrusci, A.; Stranks, S.D.; Docampo, P.; Yip, H.-L.; Jen, A.K.Y.; Snaith, H.J. High-Performance Perovskite-Polymer Hybrid Solar Cells via Electronic Coupling with Fullerene Monolayers. *Nano Lett.* **2013**, *13*, 3124–3128. [[CrossRef](#)]
27. Sarkar, A.; Jeon, N.J.; Noh, J.H.; Seok, S.I. Well-Organized Mesoporous TiO₂ Photoelectrodes by Block Copolymer-Induced Sol-Gel Assembly for Inorganic-Organic Hybrid Perovskite Solar Cells. *J. Phys. Chem. C* **2014**, *118*, 16688–16693. [[CrossRef](#)]
28. Okamoto, Y.; Fukui, R.; Fukazawa, M.; Suzuki, Y. SrTiO₃/TiO₂ composite electron transport layer for perovskite solar cells. *Mater. Lett.* **2017**, *187*, 111–113. [[CrossRef](#)]
29. Okamoto, Y.; Suzuki, Y. Mesoporous BaTiO₃/TiO₂ Double Layer for Electron Transport in Perovskite Solar Cells. *J. Phys. Chem. C* **2016**, *120*, 13995–14000. [[CrossRef](#)]
30. Apostolopoulou, A.; Sygkridou, D.; Rapsomanikis, A.; Kalarakis, A.N.; Stathatos, E. Enhanced performance of mesostructured perovskite solar cells in ambient conditions with a composite TiO₂-In₂O₃ electron transport layer. *Solar Energy Mater. Solar Cells* **2017**, *166*, 100–107. [[CrossRef](#)]
31. Kim, B.J.; Kim, D.H.; Lee, Y.-Y.; Shin, H.-W.; Han, G.S.; Hong, J.S.; Mahmood, K.; Ahn, T.K.; Joo, Y.-C.; Hong, K.S.; et al. Highly efficient and bending durable perovskite solar cells: Toward a wearable power source. *Energy Environ. Sci.* **2015**, *8*, 916–921. [[CrossRef](#)]
32. Kim, H.; Ou, K.-L.; Wu, X.; Ndione, P.F.; Berry, J.; Lambert, Y.; Mélin, T.; Armstrong, N.R.; Graham, S. Investigation of ultra-thin titania films as hole-blocking contacts for organic photovoltaics. *J. Mater. Chem. A* **2015**, *3*, 17332–17343. [[CrossRef](#)]
33. Deng, X.; Wilkes, G.C.; Chen, A.Z.; Prasad, N.S.; Gupta, M.C.; Choi, J.J. Room-Temperature Processing of TiO_x Electron Transporting Layer for Perovskite Solar Cells. *J. Phys. Chem. Lett.* **2017**, *8*, 3206–3210. [[CrossRef](#)] [[PubMed](#)]
34. Wang, J.T.-W.; Ball, J.M.; Barea, E.M.; Abate, A.; Alexander-Webber, J.A.; Huang, J.; Saliba, M.; Mora-Sero, I.; Bisquert, J.; Snaith, H.J.; et al. Low-Temperature Processed Electron Collection Layers of Graphene/TiO₂ Nanocomposites in Thin Film Perovskite Solar Cells. *Nano Lett.* **2014**, *14*, 724–730. [[CrossRef](#)] [[PubMed](#)]
35. Yang, M.; Wang, Y.; Ren, Y.; Liu, E.; Fan, J.; Hu, X. Zn/Cd ratio-dependent synthetic conditions in ternary ZnCdS quantum dots. *J. Alloys Compd.* **2018**, *752*, 260–266. [[CrossRef](#)]
36. Poormohammadi-Ahandani, Z.; Habibi-Yangjeh, A. Fast, green and template-free method for preparation of Zn_{1-x}Cd_xS nanoparticles using microwave irradiation and their photocatalytic activities. *Phys. E Low-Dimens. Sys. Nanostruct.* **2010**, *43*, 216–223. [[CrossRef](#)]
37. Gregory, D.G.; Lu, L.; Kiely, C.J.; Snyder, M.A. Interfacial Stabilization of Metastable TiO₂ Films. *J. Phys. Chem. C* **2017**, *121*, 4434–4442. [[CrossRef](#)]
38. Shi, Y.; Xing, Y.; Li, Y.; Dong, Q.; Wang, K.; Du, Y.; Bai, X.; Wang, S.; Chen, Z.; Ma, T. CH₃NH₃PbI₃ and CH₃NH₃PbI_{3-x}Cl_x in Planar or Mesoporous Perovskite Solar Cells: Comprehensive Insight into the Dependence of Performance on Architecture. *J. Phys. Chem. C* **2015**, *119*, 15868–15873. [[CrossRef](#)]
39. Sanglee, K.; Chuangchote, S.; Chaiwiwatworakul, P.; Kumnorkaew, P. PEDOT:PSS Nanofilms Fabricated by a Nonconventional Coating Method for Uses as Transparent Conducting Electrodes in Flexible Electrochromic Devices. *J. Nanomater.* **2017**, *2017*, 8. [[CrossRef](#)]
40. Levine, I.; Nayak, P.K.; Wang, J.T.-W.; Sakai, N.; Van Reenen, S.; Brenner, T.M.; Mukhopadhyay, S.; Snaith, H.J.; Hodes, G.; Cahen, D. Interface-Dependent Ion Migration/Accumulation Controls Hysteresis in MAPbI₃ Solar Cells. *J. Phys. Chem. C* **2016**, *120*, 16399–16411. [[CrossRef](#)]
41. Heo, J.H.; Han, H.J.; Kim, D.; Ahn, T.K.; Im, S.H. Hysteresis-less inverted CH₃NH₃PbI₃ planar perovskite hybrid solar cells with 18.1% power conversion efficiency. *Energy Environ. Sci.* **2015**, *8*, 1602–1608. [[CrossRef](#)]
42. Habisreutinger, S.N.; Noel, N.K.; Snaith, H.J. Hysteresis Index: A Figure without Merit for Quantifying Hysteresis in Perovskite Solar Cells. *ACS Energy Lett.* **2018**, *3*, 2472–2476. [[CrossRef](#)]
43. Zhao, Y.L.; Barman, A.R.; Dhar, S.; Annadi, A.; Motapothula, M.; Wang, J.; Su, H.; Breese, M.; Venkatesan, T.; Wang, Q. Scaling of flat band potential and dielectric constant as a function of Ta concentration in Ta-TiO₂ epitaxial films. *AIP Adv.* **2011**, *1*, 022151. [[CrossRef](#)]

44. Demiryont, H.; Nietering, K.E.; Surowiec, R.; Brown, F.I.; Platts, D.R. Optical properties of spray-deposited tin oxide films. *Appl. Opt.* **1987**, *26*, 3803–3810. [[CrossRef](#)] [[PubMed](#)]
45. Kahn, A. Fermi level, work function and vacuum level. *Mater. Horiz.* **2015**, *3*, 7–10. [[CrossRef](#)]



© 2019 by the authors. Licensee MDPI, Basel, Switzerland. This article is an open access article distributed under the terms and conditions of the Creative Commons Attribution (CC BY) license (<http://creativecommons.org/licenses/by/4.0/>).